Smart Structures and Systems, *Vol. 36, No. 3 (2025) 167-177*
https://doi.org/10.12989/sss.2025.36.3.167

Grout compactness detection of grouted splice sleeve (GSS) connector based on damping effect induced ultrasonic wave attenuation

Dongdong Chen*[1], Xiaojie Yue [1], Juntao Fan [2] and Haorun Xu [3a]

[1] *College of Civil Engineering, Nanjing Forestry University, Nanjing, Jiangsu, 210037, P.R. China*
[2] *CITIC Construction Co., Ltd., Beijing, 100027, P.R. China*
[3] *School of Aerospace Engineering and Applied Mechanics, Tongji University, Shanghai, 200092, P.R. China*

(*Received July 1, 2024, Revised August 12, 2025, Accepted August 28, 2025*)

Abstract. As an important connection component for prefabricated concrete (PC) structures, grouted splice sleeve (GSS) connectors are widely employed in building construction. However, effectively detecting grouting defects in GSS connectors remains challenging due to their concealed and inaccessible nature. This paper proposes a novel grouting defect detection method based on damping effect-induced ultrasonic wave attenuation. Based on one degree-of-freedom (DOF) free vibration system, an ultrasonic propagation absorption attenuation model considering the damping effect is built. The result indicates that the response of the model is exponentially decaying. Compared to the empty case, 90% of the ultrasonic energy is dissipated when the ultrasonic waves propagate in a compact GSS. To validate the feasibility of the detection principle, five grouting compactness cases (0%, 28%, 50%, 72%, and 100%) were artificially mimicked and tested. To improve the Signal-to-Noise Ratio (SNR), the time reversal algorithm was applied. The normalized amplitude of the focused signal in the time domain is used as an index to quantitatively reveal the compactness of GSS connectors. Experimental results confirmed that grout material significantly enhances damping effects. In addition, the damping ratios of the GSS connector and the grouting stuffing were experimentally investigated based on the logarithmic decrement of ultrasonic wave. A 2D numerical model verified that grout-induced damping causes exponential ultrasonic attenuation, aligning with theoretical predictions and experimental data. Therefore, the proposed damping effect-induced ultrasonic wave attenuation is viable for grouting compactness detection.

Keywords: damping effect; grouting defect; PZT; time reversal; wave attenuation

1. Introduction

To promote the modernization of the construction industry, prefabricated concrete (PC) structures have been rapidly developed worldwide in recent years (Zairul 2021). These structures encompass diverse forms, including frame structures, shear-wall structures, and prestressed systems, and have been extensively applied in shopping malls, parking facilities, low- and medium-rise buildings, and bridges. Compared to cast-in-situ concrete, PC structures offer significant advantages in energy conservation, environmental sustainability, shortened construction periods, and enhanced thermal insulation (Jayawardana *et al*. 2023). Although the PC structures have attracted more attention, the seismic performance of the PC structures is significant depending on the connection strength of the fabricated structural nodes. Therefore, the quality of inter-component connections is paramount to ensuring structural integrity and safety.

To date, common connection methods in structural engineering include bolted connections (Chen *et al*. 2022, Samantaray *et al*. 2018, Meher *et al*. 2022), welded connections (Kiamanesh *et al*. 2010, Ricles *et al*. 2002), slurry-anchor lap connections (Chen *et al*. 2020), and grouting sleeve connections (Kataoka *et al*. 2017). Among these, grouting sleeve connections are extensively adopted for concrete shear walls in prefabricated structures due to their high strength and simplified installation (Kahama *et al*. 2021). Specifically, this method involves inserting steel rebars into a hollow sleeve and injecting high-strength, slightly expansive grout between the sleeve and rebar. After the grouting material sets and hardens, normal stress develops at the grout-sleeve interface while frictional forces arise at the grout-rebar interface, enabling axial stress transfer. The integrated system of sleeve, rebar, and grout collectively resists structural loads. Consequently, ensuring grout compactness in sleeve joints is critical for quality control in PC structures, directly influencing joint integrity and structural safety (Lutz and Gergely 1967). However, incomplete grout filling remains a prevalent construction issue (Kim 2012), compromising axial force transmission. As concealed elements, sleeve defects are visually undetectable, making non-destructive evaluation of grouting defects particularly challenging (Ling *et al*. 2016). Research indicates that defect lengths exceeding 42 mm alter failure modes from rebar tensile failure to anchorage failure, severely jeopardizing structural safety.

To ensure the construction quality of the PC structures, it is necessary to inspect the grouting compactness of GSS

*Corresponding author, Ph.D., Associate Professor,
E-mail: chendongjt@163.com
[a] Ph.D. Student

ISSN: 1738-1584 (Print), 1738-1991 (Online)

connectors. Traditional destructive methods require drilling at detection points—a time-consuming and labor-intensive process—limiting application to selective spot checks. In recent years, non-destructive testing technologies have advanced rapidly. Approaches, including the embedded sensor method (Martínez and Andrade 2009), impact-echo method (Mori *et al*. 2002, Yue 2023), borehole endoscopy method (Fuławka *et al*. 2018), infrared thermal imaging method (Sakagami and Kubo 2002), and X-ray digital imaging method were proposed (Migeon *et al*. 1998). Thakur *et al*. (2011) employed all-fiber embedded sensors to monitor grouting completeness during construction, demonstrating effective compactness detection with temperature insensitivity. However, grout adhesion to sensors may compromise accuracy. Muldoon *et al*. (2007) tested a series of standard concrete beams with built-in plastic conduits using impact echo-based stack imaging of spectral amplitudes. The experimental results showed that the proposed method can effectively detect cavities in plastic conduits. Xie *et al*. (2022) used the borehole endoscope method to detect the sleeve in the shear wall, and the test results showed that the proposed method were direct and reliable, and the grouting defects of the sleeve could be found. Gao *et al*. (2017) achieved cross-sectional visualization of grout distribution using X-ray imaging, though radioactivity constraints limit practical deployment.

Due to its advantages of good directivity, no-radioactivity, and high resolution (Xie *et al*. 2024), ultrasonic testing has been extensively applied in concrete structures for concrete strength assessment (Bogas *et al*. 2013), concrete thickness measurement (Trtnik *et al*. 2009), concrete defects detection (Dang *et al*. 2023, Saint-Pierre *et al*. 2016). A total focusing method (TFM) based on ultrasonic waves is employed by Liu *et al*. (2023) for debonding damage detection in concrete-filled steel tube (CFST) structures. 16 CFST columns of the Shenzhen SEG Building were successfully inspected and the result shows that the comprehensive debonding rate is about 46.6%. The ultrasonic wave can also be used in grout compactness detection of GSS connectors. Jiang and Cai (2018) derived the first-arriving ultrasonic wave propagation path and proposed the t-distribution-based ultrasonic probability algorithm for compactness detection of GSS connectors. Qu *et al*. (2021) investigated compactness tomography using ultrasonic waves. Finite element simulations and experimental testing were carried out in their research. A validation experiment was carried out and five grouted defects in five GSS connectors were investigated. Li *et al*. (2019) presented the guided wave waveforms at different grouting defects, and a damage index was proposed by calculating the differences between compactness and defective specimens. A wavelet packet energy algorithm was proposed by Cao *et al*. (2023) for testing the compactness of grouting sleeves. Finite element analysis of ultrasonic elastic wave propagation was performed and the energy proportion distribution shows that the high-frequency component gradually decreases with the decrease of anchorage length.

Although previous studies have demonstrated the feasibility of ultrasonic-based grouting compactness detection, the mechanism is not fully revealed. This paper proposes a novel defect detection approach based on damping effect-induced ultrasonic wave attenuation. By modeling the transducer-specimen system as a one degree-of-freedom (DOF) free vibration system, the system response under ultrasonic excitation with damping effects can be derived. Experimental validation employed five full-scale GSS connectors with surface-mounted Lead Zirconate Titanate (PZT) transducers, complemented by a 2D numerical model to elucidate the detection principle. The paper is organized as follows: section 2 presents the theoretical principles derived from the damping model. Section 3 details experimental validation. Section 4 conducts numerical simulations of damping effects on ultrasonic propagation. Section 5 provides concluding remarks.

2. Detection principles based on damping effect

Assuming the PZT-based pitch-catch system as a one degree-of-freedom (DOF) free vibration system, the governing equation can be expressed as Eq. (1)\

$$m\ddot{x}(t) + c\dot{x}(t) + kx(t) = F(t) \tag{1}$$

where $x(t)$ is the displacement with the variation of time t, $F(t)$ is external force, m, c, and k are the mass, damping, and stiffness of the structures, respectively.

Eq. (1) is the expression of a forced vibration system. To obtain the solution of the equation, the free vibration should be studied first, as shown in Eq. (2)

$$m\ddot{x}(t) + c\dot{x}(t) + kx(t) = 0 \tag{2}$$

The solution of free vibration can be assumed as

$$x(t) = Ge^{st} \tag{3}$$

where G is a complex constant, e^{st} is an exponential function.

Substituting Eq. (3) into Eq. (2) yields

$$(s^2 + \frac{c}{m}s + \omega^2)Ge^{st} = 0 \tag{4}$$

The solution for Eq. (4) can be expressed as

$$s_{1,2} = -\frac{c}{2m} \pm \sqrt{\left(\frac{c}{2m}\right)^2 - \omega^2} \tag{5}$$

In practice, the damping ratio—defined as the ratio of a system's actual damping to its critical damping—provides a convenient metric for quantifying energy dissipation. When externally excited, a vibrating structure exhibits amplitude attenuation due to dissipative forces that progressively decay its motion. This ratio physically characterizes the amplitude reduction extent and critically determines vibration system stability and energy transfer efficiency.

Eq. (6) shows the expression of the damping ratio

$$\xi = \frac{c}{2m\omega} \tag{6}$$

where $\omega = \sqrt{\frac{k}{m}}$ is the circular frequency.

For the low damping system, the solution of s in Eq. (5) can be obtained by substituting Eq. (6) into Eq. (5)

$$s_{1,2} = -\xi\omega \pm i\omega\sqrt{1-\xi^2} \tag{7}$$

The solution of free vibration can be expressed as

$$x(t) = \rho\, cos(\,\omega t\sqrt{1-\xi^2} + \theta)e^{(-\xi\omega t)} \tag{8}$$

Eq. (8) is the solution of Eq. (2), which is the general solution of the one degree-of-freedom (DOF) forced vibration system in Eq. (1).

Although Eq. (8) shows the specific relationship between the $x(t)$ and the damping ratio ξ, the damping ratio's physical influence requires further interpretation. Therefore, to fully understand the influence of the damping ratio, a numerical analysis was performed. Ten values, from 0.01 to 0.10 with an interval of 0.01 were calculated. Specifically, in the numerical analysis, t = 0.002 s, the amplitude of the constant term of ρ is normalized. The circular frequency is 228 kHz, which corresponds to the central frequency of the excited signal in the experimental validation in section 3. The phase angle is 0. As shown in Fig. 1, as the increase of damping ratio, the amplitudes of the normalized displacement decay increasingly. When the ξ is 0.01, it took more than 2 μs for the amplitude of the normalized displacement to decay from 1 to 0. However, it took about 0.3 μs when the ξ equal to 0.1. Thus, higher damping ratios correspond to stronger damping forces, accelerating amplitude decay and equilibrium restoration. Conversely, lower damping ratios reduce dissipation forces, prolonging both amplitude decay and system stabilization. These results confirm the damping ratio's critical role in governing structural response dynamics.

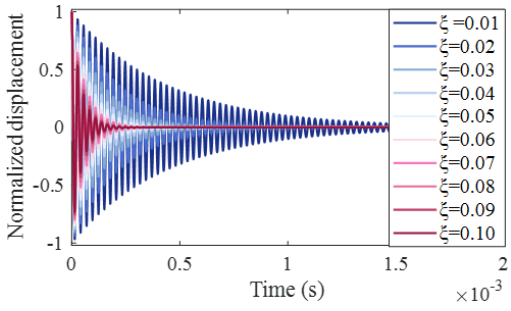

Fig. 1 Free vibration of low damping system with different damping ratio

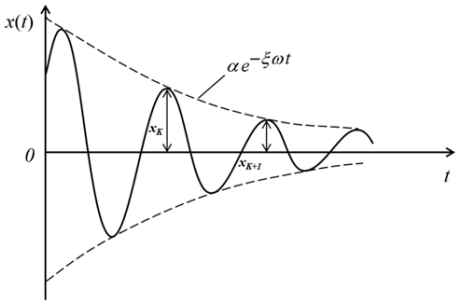

Fig. 2 Schematic diagram of low damping free vibration

For the low damping system (the damping is lower than the critical damping, $\xi < 1$), the schematic diagram of low damping free vibration is presented in Fig. 2. In this case, the damping ratio of the system can be solved using the free vibration damping method.

$$\xi = \frac{1}{2\pi} ln \frac{x_K}{x_{K+1}} \tag{9}$$

where the x_K and x_{K+1} are the two adjacent peaks in the free decay curves, respectively. $ln\frac{x_K}{x_{K+1}}$ is the logarithmic decrement of the vibration amplitude. Considering nth peaks in a vibration process, Eq. (9) can be expressed as follows

$$\xi = \frac{1}{2\pi n} ln \frac{x_K}{x_{K+n}} \tag{10}$$

where x_{K+n} is the amplitude of nth wave peak after x_K in the free decay curve.

Assuming that $\{S_0\}$, $\{S_1\}$, …, $\{S_N\}$ are the recorded ultrasonic signal at nth different grouting compactness, $\{A_0\}$, $\{A_1\}$, …, $\{A_N\}$ are the amplitudes of the $\{S_0\}$, $\{S_1\}$, …, $\{S_N\}$, respectively. To quantitatively evaluate the compactness of grouted splice sleeve (GSS), a compactness index based on the normalized amplitude of wave signal in time domain was proposed, as shown in Eq. (11)

$$DI^i = \frac{A_i}{A_0} \tag{11}$$

where the A_i is the amplitude of $\{S_i\}$, (i = 1, 2, ..., N).

3. Experiment

3.1 Specimen and setup

Five full-scale GSS connectors were tested (Fig. 3), with inner and outer diameters of 36 mm and 48 mm respectively, and a length of 310 mm. Embedded rebars measured 16 mm in diameter. Fig. 4 details the GSS dimensions and PZT transducer locations. The grouting material comprises a high-strength, non-shrinking composition with a water-to-cement ratio of 1:0.14. Table 1 summarizes its key parameters.

Grouting defects predominantly occur near the outlet due to leakage from the bottom inlet. Accordingly, PZT

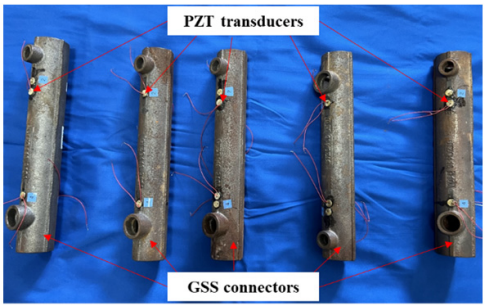

Fig. 3 Five whole GSS connectors

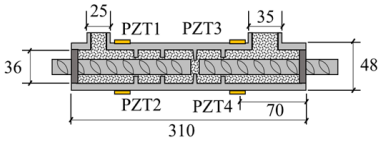

Fig. 4 The dimension of the GSS connector (unit: mm)

Table 1 Parameters of high strength grouting material

Index	Critical value	Observed data
Fluidity/mm	Initial	305
	30 min	275
Compressive strength/Mpa	1 d	30.1
	3 d	47.5
Vertical expansion rate	3 h	0.14
	Deviation between 24 h and 3 h	0.06
Chloride ion content/%	-	0.01
Bleeding rato/%	-	0

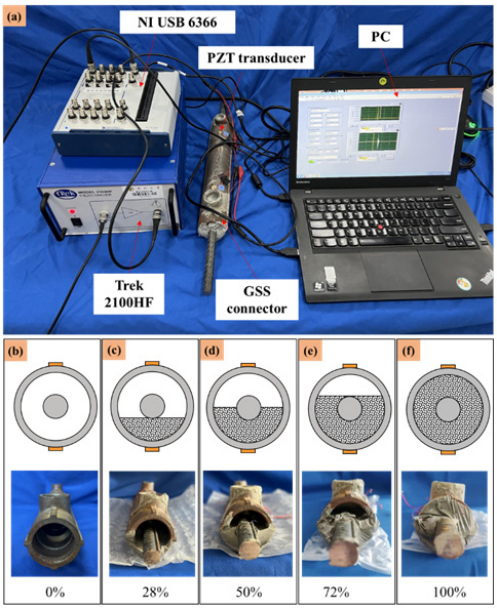

Fig. 5 Experimental setups (a) and (b) grouting cases 1 (0%); (c) grouting case 2 (28%); (d) grouting case 3 (50%); (e) grouting case 4 (72%); (f) grouting case 5 (100%)

transducers were mounted at two strategic locations: adjacent to the inlet and outlet. Implementing the pitch-catch strategy defined by our detection principles, four PZT transducers (diameter: 10 mm, thickness: 1 mm) were affixed to opposite sides of the GSS outer surface. PZT1 and PZT3 functioned as actuators, while PZT2 and PZT4 served as sensors. Although grout strength increases with curing age, sleeve bearing capacity reaches 96% of ultimate strength after 7 days, with subsequent strength gain diminishing significantly. Thus, ultrasonic signal acquisition was conducted precisely 7 days post-grouting.

As shown in Fig. 5(a), a PC equipped with LabVIEW software platform was used to control the NI USB 6366 data acquisition (DAQ) card to pulse the excite signal and record the propagating wave. A power amplifier (Trek model 2100 HF) was used to amplify the signal output from NI USB 6366. Five grouting compactness cases, including 0%, 28%, 50%, 72%, and 100% were artificially mimicked, as shown in Figs. 5(b)-(f).

The pulse signal is a modulated Gaussian signal, which can be expressed as

$$x(t) = A_G e^{-k_e(t-d)^2} cos(2\pi f_c(t-d)) \tag{12}$$

$$k_e = \frac{5\pi^2 b^2 {f_c}^2}{q\, ln(10)} \tag{13}$$

where A_G is the amplitude, d denotes the time delay, f_c is the central frequency, b represents the normalized bandwidth, and q is the attenuation constant.

The parameters of the Gaussian pulse are shown in Table 2. It should be noted that before pulsing the Gaussian signal, the excitation frequency should be specified. To determine the central frequency of the emitted pulse signal, a linear sweep signal ranging from 1 kHz to 500 kHz was applied to the PZT actuator. Fig. 6(a) is the received signal from PZT2. Fast Fourier transform (FFT) was used to extract the resonant frequency of the recorded signal, as shown in Fig. 6(b). The result shows that the central frequency is about 228.8 kHz.

Due to the strong energy dissipation effect, the amplitude of the received signal is very low. To improve the SNR, time reversal algorithm was applied in the experiment. The procedure of the time reversal process is shown in Fig. 7. Taking PZT3 and PZT4 as an example, the time reversal process can be described as follows:

(1) PZT3 was excited by the Gaussian pulse signal.
(2) PZT4 senses and records the ultrasonic wave propagated from the waveguide (steel sleeve and inner grouting stuffing).
(3) The recorded signal in step (2) was reversed in time domain and reemitted by PZT4.

Table 2 Sweep signal parameters of Gaussian pulse

Central frequency (kHz)	Amplitude (V)	Sampling frequency (MHz/s)	Attenuation (dB)	Normalized bandwidth (kHz)
228.8	1	2	0.8	1.5

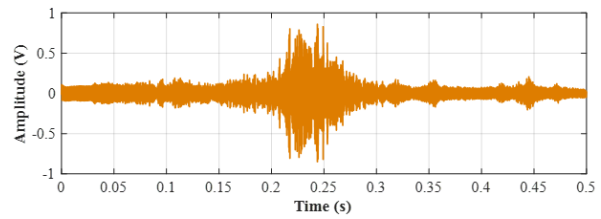

(a)

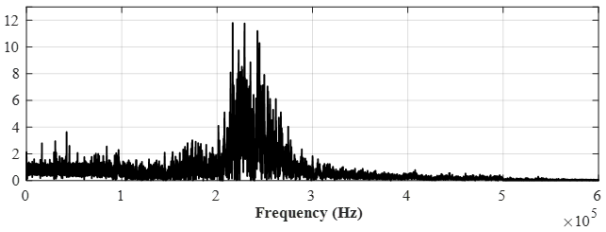

(b)

Fig. 6 The received signal in (a) time domain; and (b) frequency domain

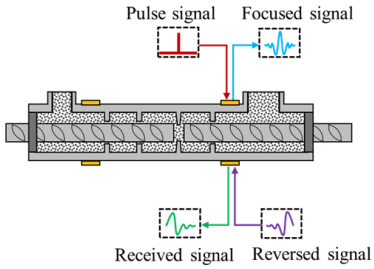

Fig. 7 Schematic diagram of the time reversal process

(4) PZT3 senses the ultrasonic wave reemitted by PZT4. The signal has the characteristic of temporal and spatial focusing characteristics.

3.2 Experimental result

Fig. 8 illustrates the time reversal process signals for the fully grouted case. Fig. 8(a) shows the Gaussian pulse signal applied to the actuator, while Fig. 8(b) displays the sensed signal recorded by the PZT sensor, with an amplitude of 0.021 V. Following time reversal processing, the received signal is amplified 10 times and retransmitted. Fig. 8(d) presents the resulting focused signal, which exhibits an amplitude approximately twice that of the direct-arrival signal in Fig. 8(b). Thus, the TR algorithm significantly enhances the SNR of ultrasonic waves, particularly in high-attenuation environments.

In this experiment, two detection spots were designated per GSS connector, resulting in ten total detection points across five specimens with PZT transducers attached. However, signals from two PZTs failed to capture ultrasonic waves, leaving eight locations available for analysis. Due to variations in bonding thickness, weld quality, and other installation factors between transducers, signal amplitudes differed across PZTs. To isolate the attenuation effects of grout defects, the focused signal amplitudes were normalized. Fig. 9 presents the normalized amplitudes for all five grouting conditions following time reversal processing.

As shown in Fig. 9, the amplitude of the focused signal decreases with increasing grouting ratio. For the 0% grout condition (i.e., an empty GSS connector), the amplitude reaches its maximum value. However, as grout progressively fills the connector, the normalized wave energy exhibits significant attenuation. At 50% grouting ratio, the amplitude is reduced to less than 50% of the 0% grouting case value. In the fully grouted condition (100% fill), 98% of the signal amplitude is attenuated, demon-strating that the grouting material dissipates most ultrasonic wave energy through damping mechanisms. The damage index (DI) values decrease exponentially with grouting ratio, following the

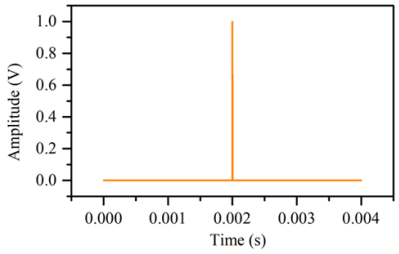

(a)

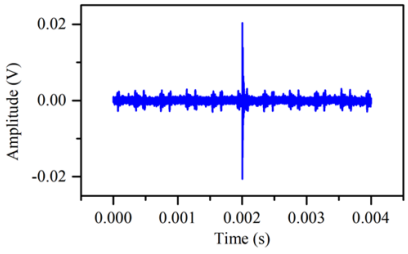

(b)

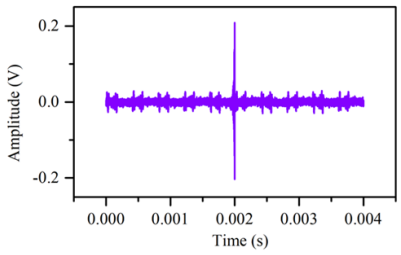

(c)

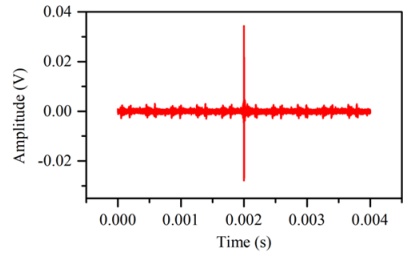

(d)

Fig. 8 (a) Gaussian pulse; (b) received signal; (c) reversed signal; and (d) focused signal in time reversal process at full grouting case

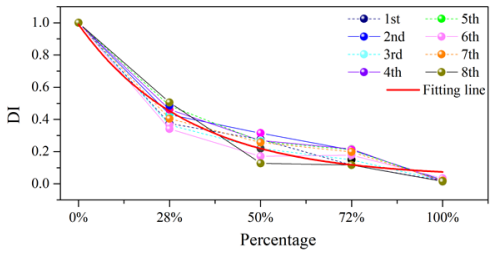

Fig. 9 DI values for five grouting compactness

fitting function

$$f(p) = -4.61 \times 10^{-4} + 0.993e^{(-\frac{p-0.078}{34.670})} \quad (14)$$

where the p is the grouting percentage. In addition, the coefficient of determination (R^2) is 0.970, indicating the exponential decay curve is well fitted to the experimental result.

The variance and the standard deviation were calculated in our revised manuscript and the results were presented in Table 3. Table 3 shows that when the grouting percentage is 50%, the maximum variance is 0.0033, and the standard deviation is 0.057, which also reaches the maximum value.

To characterize frequency responses across grouting conditions, fast Fourier transform (FFT) analysis was performed on the 0%, 50%, and 100% cases. As shown in Fig. 10, in the empty GSS connector condition, ultrasonic waves propagate unimpeded along the sleeve, yielding a central frequency band of 180–280 kHz. As the grouting compactness increases to 50%, the amplitude of the high-frequency component decreases significantly. When the GSS connector is fully compact, the central frequency is about 1.45 kHz, and the high-frequency component is filtered. This occurs because increased grout volume extends the wave propagation path through the material, where reflection, refraction, and scattering dissipate wave energy. Consequently, the grouting medium functions as a low-pass filter, selectively attenuating high-frequency components during waveguide propagation.

Table 3 Variation and standard deviation for different grouting percentage

Percentage (%)	0	28	50	72	100
Variance	0	0.0031	0.0033	0.0015	$3.8e^{-5}$
Standard deviation	0	0.056	0.057	0.040	0.0062

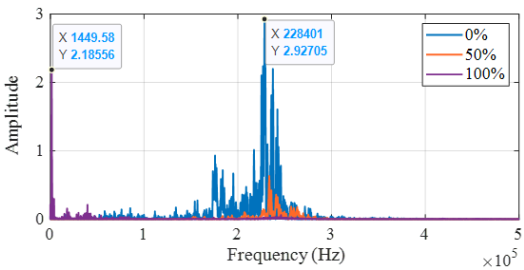

Fig. 10 Frequency for five grouting compactness

4. Numerical simulation

To elucidate the damping-based detection mechanism for grouted splice sleeves (GSS), numerical analysis was conducted, leveraging experimentally determined damping properties. Section 4.1 quantifies the damping ratios of both the GSS structure and grout through experimental testing. Building on these results, section 4.2 establishes a finite element model that simulates varying grouting conditions using the damping parameters from section 4.1. Section 4.3 presents the corresponding simulation outcomes, revealing the fundamental relationship between grout-induced damping and ultrasonic wave dissipation.

4.1 Damping tests of the grouting stuffing and GSS

Fig. 11 illustrates the experimental setup for damping characterization. A PXIe-1088 host chassis with integrated PXI-5412 oscilloscope module was used to acquire time-domain waveforms. The CTS-8077PR ultrasonic instrument (Guangdong Goworld Co., Ltd., Ultrasonic Instrument Branch) was connected to a single PZT transducer for pulse excitation and signal reception. Critically, this configuration differs from the pitch-catch arrangement in Section 3.1: whereas section 3.1 employed two transducers (one actuator, one sensor), this damping test utilized a single transducer operating in pulse-echo mode to measure free-decay ultrasonic responses. This approach enables direct acquisition of grout and GSS free-decay curves, thereby allowing precise quantification of material damping properties in both waveguide systems.

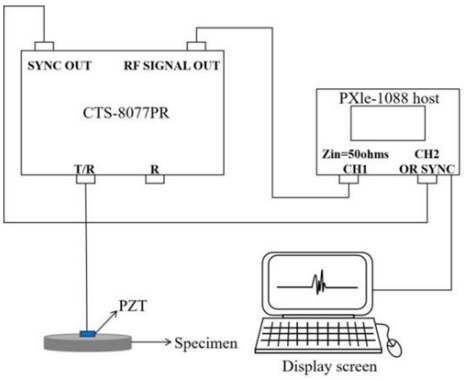

(a)

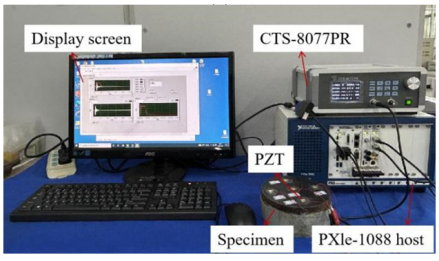

(b)

Fig. 11 Setups for damping test: (a) schematic diagram; (b) experimental test

(1) Damping ratio tests of the GSS material

Since the damping ratio of the GSS cannot be measured directly, the damping ratio of a steel plate of the same material as the GSS is used. To reduce the measurement errors in the experiment, five measuring points (PG1, PG2, PG3, PG4, and PG5) were selected, and five PZT-5H sensors were pasted onto the surface of the steel plate, as shown in Fig. 12. Taking PG1 as an example, the reflected wave in time domain for GSS damping test is presented in Fig. 13. As shown in Fig. 13, the 1st, 2nd, and 3rd reflected waves can be clearly recorded.

According to Eq. (9), x_K and x_{K+n} are the amplitudes of K^{th} and $(K+n)^{th}$ wave peaks, respectively. Since the 1st reflected wave owns the largest amplitude, the waveform of the 1st reflected wave was applied for the damping calculation of GSS material. In this research, K and n are 1 and 3, respectively. Therefore, in Fig. 13, x_1 is 1.395 V and x_4 is 0.486 V. Substituting x_1 and x_4 into Eq. (9) yields the value of the damping ratio of GSS material. The result of the damping ratio of the GSS material is shown in Table 4. The average damping ratio of GSS material in this research is 0.057.

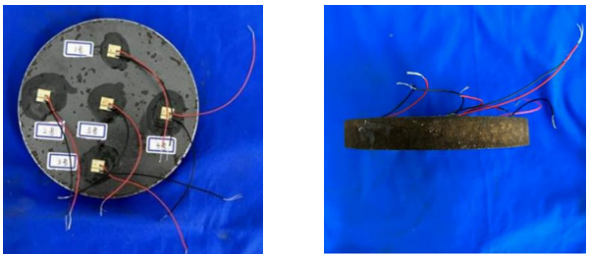

(a) (b)

Fig. 12 Specimen for GSS damping test in (a) vertical; and (b) side views

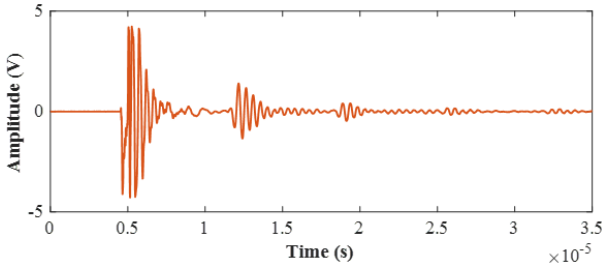

Fig. 13 Reflected wave in time domain for GSS damping test

Table 4 Damping ratio of the GSS material

Test point	PG1	PG2	PG3	PG4	PG5	Average
Value (10^{-2})	5.59	6.17	5.21	5.51	6.02	5.70

Table 5 Damping ratio of the grouting stuffing

Test point	PG1	PG2	PG3	PG4	PG5	Average
Value (10^{-2})	8.2	7.91	8.11	8.18	7.99	8.s08

(2) Damping ratio tests of the grouting stuffing

A cylindrical specimen (radius: 72.5 mm, height: 43 mm) was fabricated using the same grout mixture and water-to-cement ratio as section 3.1. After 7-day standard curing, damping ratios were measured via free-decay testing. To minimize measurement uncertainty, five measuring points (PS1, PS2, PS3, PS4, and PS5) were selected, and five PZT-5H sensors were pasted onto the surface of the specimen, as shown in Fig. 14. The reflected wave recorded by PG1 is presented in Fig. 15.

As shown in Fig. 15, due to the significant energy dissipation effect of the grouting stuffing damping, only the 1st reflected wave can be observed in the reflected wave. In this section, K and n are 1 and 2, respectively. Therefore, x_1 is 0.1278 V and x_3 is 0.0473 V. Substituting x_1 and x_3 into Eq. (9), the damping ratio of grouting stuffing can be obtained. The damping ratio of the grouting stuffing in five repeated tests is shown in Table 5. The average damping ratio of grouting stuffing is 0.808, which is 1.42 times that of the GSS material.

4.2 Multi-physics field coupling modelling

In this section, a two-dimension GSS model was built using COMSOL Multiphysics. Seven grouting levels, including 0%, 14%, 28%, 50%, 72%, 86%, and 100% were considered. As shown in Table 6.

To accurately simulate the wave propagating process in GSS connectors, five components, including two PZT

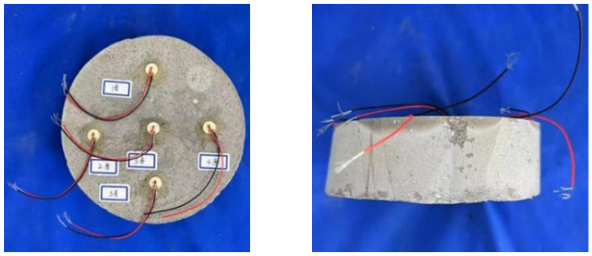

(a) (b)

Fig. 14 Specimen for grouting stuffing damping test in (a) vertical view; and (b) side view

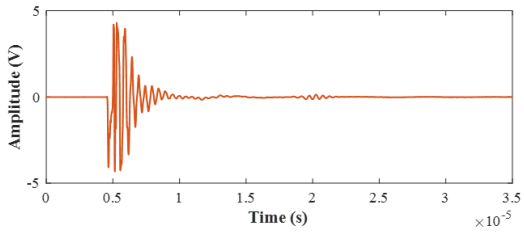

Fig. 15 Reflected wave in time domain for grouting stuffing damping test

Table 6 Grouting levels in coupling modeling

Cases	G1	G2	G3	G4	G5	G6	G7
Grouting levels (%)	0	14	28	50	72	86	100

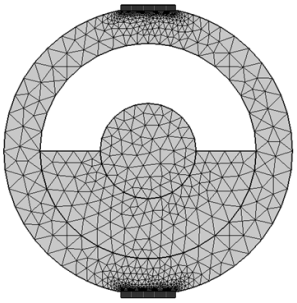

Fig. 16 Finite element model of GSS in G4 (50% grouting level)

transducers (PZT1, and PZT2), splice sleeve, grouting, and steel bar, were built in the numerical model. Taking the grouting case of G4 as an example, Fig. 16 is the finite element model of GSS. In our model, PZT1 and PZT2 are mounted on the bottom and top surface of the splice sleeve, and the thin epoxy layer is not considered. All the components are connected by Form Union. Two physical field modules, the solid mechanics field and the electrostatic field are applied. A Gaussian signal which is the same as section 3 is modulated. The modulated Gaussian signal is excited by PZT1 with an amplitude of 50 V. The upper surface of the PZT2 is set to a terminal. Two mesh cell types, free triangular grid and rectangular grid are applied. For the balance of calculation time and efficiency, the element size is less than 1/10 of the wavelength and the maximum integration step size should be less than 1/20 of the maximum period. Splice sleeves, grouting stuffing and steel bars were assumed to be isotropic materials. The damping ratio of the GSS material and grouting stuffing measured in section 4.1 were applied in the simulation. Table 7 shows the parameters of the material properties.

Table 7 Material properties of splice sleeves, steel bar and grouting stuffing

Material	Density ($kg•m^{-3}$)	Elastic modulus (104 MPa)	Poisson's ratio	Damping ratio
Splice sleeves and steel bar	7850	20.5	0.2	0.057
Grouting stuffing	2300	2.5	0.28	0.081

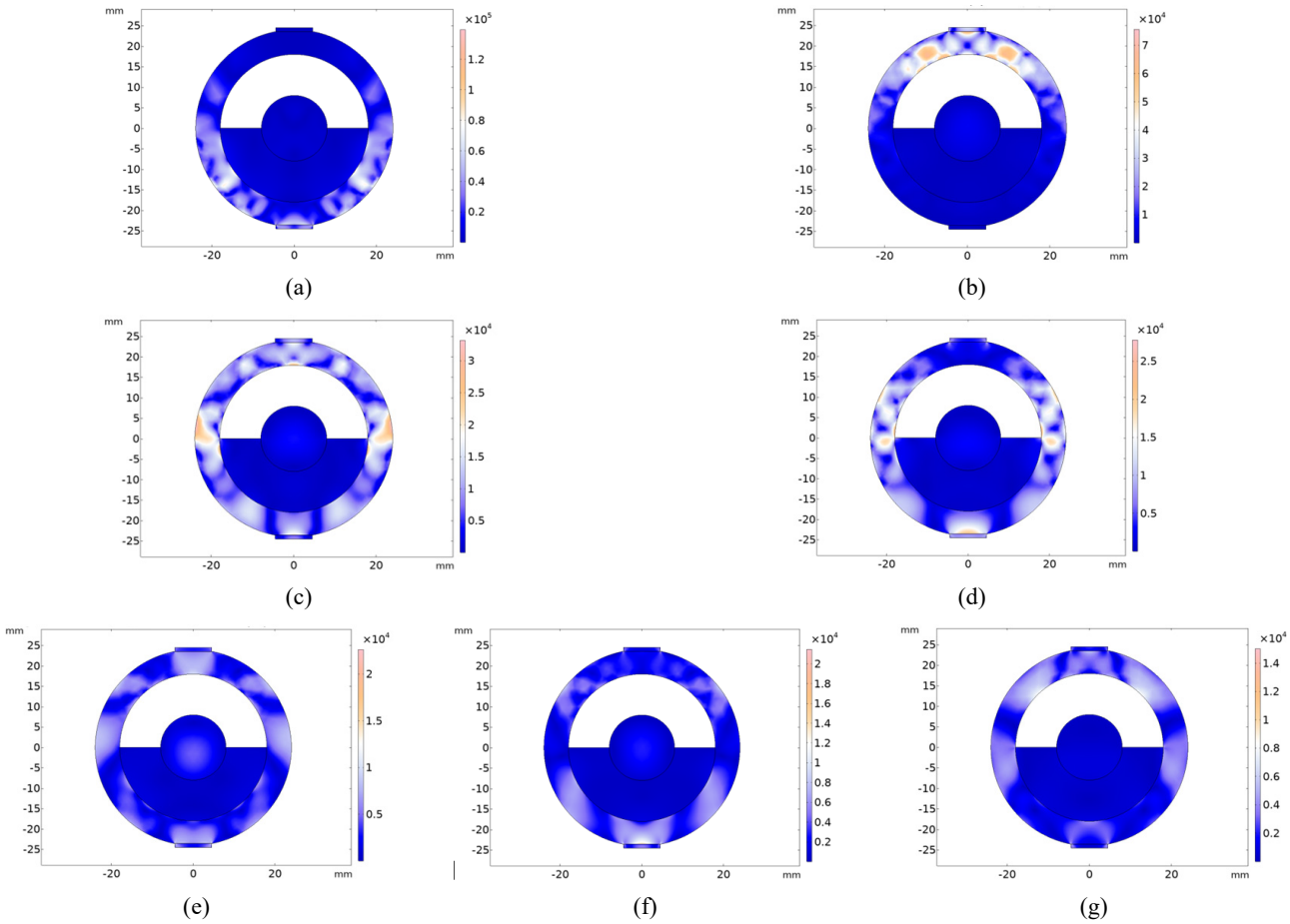

Fig. 17 Schematic of the stress field at (a) t = 1e-5 s; (b) t = 2e-5 s; (c) t = 3e-5 s; (d) t = 4e-5 s; (e) t = 5e-5 s; (f) t = 6e-5 s; and (g) t = 7e-5 s

4.3 Result

Signals received by PZT2 reveal ultrasonic wave propagation through the GSS connector across varying grouting levels (Fig. 17). Due to significantly higher wave velocity in steel compared to grout, waves reach the sleeve's upper region by $t = 1 \times 10^{-5}$ s. The low damping ratio of steel further confines propagation primarily within the sleeve walls, as evidenced in Figs. 17(b)-(d). Normalized signal amplitudes (Fig. 18) demonstrate maximum amplitude occurring in non-grouted specimens. Simulation results incorporating time reversal processing yielded focused time-domain signals for seven grouting cases (Fig. 19), with extracted compactness indices plotted in Fig. 20. These results confirm an exponential amplitude decay with increasing grout volume, expressed as

$$f(p) = 0.123 + 0.903e^{\left(-\frac{p+0.411}{11.549}\right)} \quad (15)$$

The coefficient of determination (R^2) in Fig. 20 is 0.973. The exponential decay curve fits well with the simulation results. In addition, the simulation results are consistent with the experimental results, which verifies the reliability of the simulation results. Therefore, the normalized amplitude can function as an indicator to quantitatively reveal the compactness of the splice sleeve.

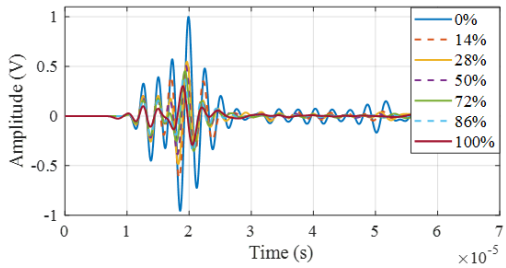

Fig. 18 Received signals after normalization with different grouting compactness levels

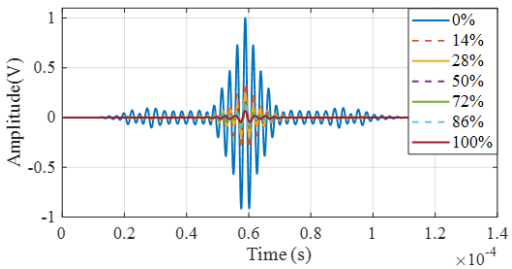

Fig. 19 Time-reversed signals after normalization with different grouting compactness levels

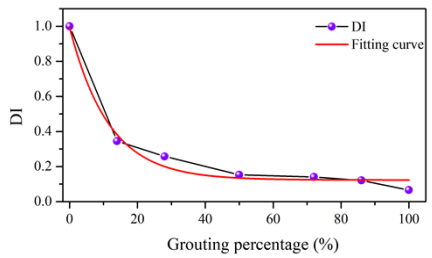

Fig. 20 Time-reversed signals after normalized in different grouting compactness

5. Discussion

Unfavorable factors, including the ambient noise, surface roughness, and inconsistent bonding of PZT sensors, are critical for practical inspection. For the ambient noise, the time reversal (TR) algorithm enhances signal-to-noise ratio (SNR) by temporally and spatially focusing ultrasonic energy. A 200% amplitude gain can be obtained after TR processing. In addition, the filter algorithms can be applied to further isolate ambient noise. Surface irregularities may affect acoustic coupling between PZT transducers and the sleeve. To address this issue, surface roughness should be treated, such as polishing. In addition, the normalized amplitude index can detect poor sensor bonding. In the future, an on-site study is planned on a prefabricated bridge, where environmental factors (e.g., temperature, humidity) and structural vibrations will be considered and monitored.

6. Conclusions

Based on the damping model, this study proposes an ultrasonic wave-based approach for grouting defect detection. The key conclusions are summarized as follows:

(1) By modeling the PZT pitch-catch system as a one degree-of-freedom (DOF) free vibration system, the detection principle using ultrasonic wave was revealed. Results demonstrate that structural responses are significantly governed by damping ratio, with 90% ultrasonic energy dissipation observed in fully compacted GSS connectors versus empty cases.

(2) Implementation of the time reversal algorithm enhanced signal-to-noise ratio (SNR), while the normalized amplitude of focused signals served as a quantitative compactness indicator. Validation experiments on five full-scale GSS connectors confirmed that grout-induced damping causes exponential ultrasonic wave attenuation.

(3) A 2D numerical model further elucidated the damping-based detection mechanism. Experimentally measured damping ratios for both GSS connectors and grout material were incorporated into the finite element model. Simulations across seven grouting cases revealed exponentially decaying normalized amplitudes with increasing grout percentage, aligning with experimental results and confirming grout-dominated ultrasonic energy dissipation.

Acknowledgments

This work was partially supported by the National Natural Science Foundation of China (NSFC) (No. 52408337), China Postdoctoral Science Foundation (No. 2023M741728), Basic Science Research of Jiangsu Province Higher Education Institution (No. 24KJB580008), the Open Research Fund of State Key Laboratory of Mountain Bridge and Tunnel Engineering (SKLBT-2106), and Nanjing Construction Industry Science and Technology Plan Project (Ks2389). The authors would like to acknowledge the financial support given to the present research.

References

Bogas, J.A., Gomes, M.G. and Gomes, A. (2013), "Compressive strength evaluation of structural lightweight concrete by non-destructive ultrasonic pulse velocity method", *Ultrasonics*, **53**(5), 962-972. https://doi.org/10.1016/j.ultras.2012.12.012

Cao, D., Pan, Z., Zhang, Z. and Zeng, B. (2023), "Study on non-destructive testing method of grouting sleeve compactness with wavelet packet energy ratio change", *Constr. Build. Mater.*, **389**, p. 131767. https://doi.org/10.1016/j.conbuildmat.2023.131767

Chen, J., Chen, X., Ding, F., Xiang, P., Yang, C., Liu, Y. and Xu, F. (2020), "Mechanical performance of overlap connections with grout-filled anchor reinforcements in embedded metal corrugated pipe", *Arch. Civil Mech. Eng.*, **20**(4), p. 128. https://doi.org/10.1007/s43452-020-00121-2

Chen, D., Huo, L. and Song, G. (2022a), "High resolution bolt pre-load looseness monitoring using coda wave interferometry", *Struct. Health Monitor.*, **21**(5), 1959-1972. https://doi.org/10.1177/14759217211063420

Chen, D., Huo, L. and Song, G. (2022b), "High resolution bolt pre-load looseness monitoring using coda wave interferometry", *Struct. Health Monitor.*, **21**(5), 1959-1972. https://doi.org/10.1177/14759217211063420

Chen, R., Tran, K.T., Dinh, K. and Ferraro, C.C. (2022), "Evaluation of ultrasonic sh-waveform tomography for determining cover thickness and rebar size in concrete structures", *J. Nondestr. Eval.*, **41**(2), p. 35. https://doi.org/10.1007/s10921-022-00866-1

Dang, N.L., Pham, Q.Q. and Kim, J.T. (2023), "Hybrid vibration-impedance monitoring in prestressed concrete structure with local strand breakage", *Smart Struct. Syst., Int. J.*, **30**(5), 463-477. https://doi.org/10.12989/sss.2022.30.5.463

Fuławka, K., Mertuszka, P. and Pytel, W. (2018), "Monitoring of the stability of underground workings in Polish copper mines conditions", In: *E3S Web of Conferences*, Vol. 29, p. 00008. https://doi.org/10.1051/e3sconf/20182900008

Gao, R., Li, X. and Wang, Z. (2017), "Research on testing of grouting plumpness of sleeve based on embedded steel wire drawing method", *Constr. Technol.*, **46**(17), 1-5.

Jayawardana, J., Sandanayake, M., Jayasinghe, J.A.S.C., Kulatunga, A.K. and Zhang, G. (2023), "A comparative life cycle assessment of prefabricated and traditional construction – A case of a developing country", *J. Build. Eng.*, **72**, p. 106550. https://doi.org/10.1016/j.jobe.2023.106550

Jiang, S. and Cai, W. (2018), "Ultrasonic testing method of grouting sleeve compactness", *J. Vib. Shock*, **37**(10), 43-49.

Kahama, E., Fuzhe, X. and Anglaaere, D.L.M. (2021c), "Numerical study on the influence of defects in grouting on the mechanical properties of a full grouted sleeve connector", *J. Adhes.*, **98**, 2550-2581. https://doi.org/10.1080/00218464.2021.1982389

Kataoka, M.N., Ferreira, M.A. and de Cresce El Debs, A.L.H. (2017), "Nonlinear FE analysis of slab-beam-column connection in precast concrete structures", *Eng. Struct.*, **143**, 306-315. https://doi.org/10.1016/j.engstruct.2017.04.028

Kiamanesh, R., Abolmaali, A. and Ghassemieh, M. (2010), "The effect of stiffeners on the strain patterns of the welded connection zone", *J. Constr. Steel Res.*, **66**(1), 19-27. https://doi.org/10.1016/j.jcsr.2009.07.010

Kim, H.K. (2012), "Bond strength of mortar-filled steel pipe splices reflecting confining effect", *J. Asian Archit. Build. Eng.*, **11**(1), 125-132. https://doi.org/10.3130/jaabe.11.125

Li, Z., Zheng, L., Chen, C., Long, Z. and Wang, Y. (2019), "Ultrasonic detection method for grouted defects in grouted splice sleeve connector based on wavelet pack energy", *Sensors*, **19**(7), Article 7. https://doi.org/10.3390/s19071642

Ling, J.H., Abd. Rahman, A.B., Ibrahim, I.S. and Abdul Hamid, Z. (2016), "Tensile capacity of grouted splice sleeves", *Eng. Struct.*, **111**, 285-296. https://doi.org/10.1016/j.engstruct.2015.12.023

Liu, H., Qi, Y., Chen, Z., Tong, H., Liu, C. and Zhuang, M. (2021), "Ultrasonic inspection of grouted splice sleeves in precast concrete structures using elastic reverse time migration method", *Mech. Syst. Signal Process.*, **148**, p. 107152. https://doi.org/10.1016/j.ymssp.2020.107152

Liu, H., Chen, Z., Liu, Y., Chen, Y., Du, Y. and Zhou, F. (2023), "Interfacial debonding detection for CFST structures using an ultrasonic phased array: Application to the Shenzhen SEG building", *Mech. Syst. Signal Process.*, **192**, p. 110214. https://doi.org/10.1016/j.ymssp.2023.110214

Lutz, L.A. and Gergely, P. (1967), *Mechanics of Bond and Slip of Deformed Bars in Concrete.* https://www.concrete.org/publications/internationalconcreteabstractsportal.aspx?m=details&ID=7600&m=details&ID=7600

Martínez, I. and Andrade, C. (2009a), "Examples of reinforcement corrosion monitoring by embedded sensors in concrete structures", *Cement Concrete Compos.*, **31**(8), 545-554. https://doi.org/10.1016/j.cemconcomp.2009.05.007

Meher, U., Mishra, S.K. and Sunny, M.R. (2022), "Impedance-based looseness detection of bolted joints using artificial neural network: An experimental study", **29**(10), *Struct. Control Health Monitor.*, **29**(10), p. e3049. https://doi.org/10.1002/stc.3049

Migeon, S., Weber, O., Faugeres, J.-C. and Saint-Paul, J. (1998), "SCOPIX: A new X-ray imaging system for core analysis", *Geo-Marine Letters*, **18**(3), 251-255. https://doi.org/10.1007/s003670050076

Mori, K., Spagnoli, A., Murakami, Y., Kondo, G. and Torigoe, I. (2002), "A new non-contacting non-destructive testing method for defect detection in concrete", *NDT & E Int.*, **35**(6), 399-406. https://doi.org/10.1016/S0963-8695(02)00009-9

Muldoon, R., Chalker, A., Forde, M.C., Ohtsu, M. and Kunisue, F. (2007), "Identifying voids in plastic ducts in post-tensioning prestressed concrete members by resonant frequency of impact–echo, SIBIE and tomography", *Constr. Build. Mater.*, **21**(3), 527-537. https://doi.org/10.1016/j.conbuildmat.2006.04.009

Qu, M., Shao, Z., Zhao, W. and Zha, X. (2021), "Research on nondestructive testing of grouting sleeve members by ultrasonic tomography", *Indust. Constr.*, **51**(9), 207-215. https://doi.org/10.13204/j.gyjzG21020316

Ricles, J.M., Mao, C., Lu, L.W. and Fisher, J.W. (2002), "Inelastic cyclic testing of welded unreinforced moment connections", *J. Struct. Eng.*, **128**(4), 429-440. https://doi.org/10.1061/(ASCE)0733-9445(2002)128:4(429)

Saint-Pierre, F., Philibert, A., Giroux, B. and Rivard, P. (2016), "Concretequality designation based on ultrasonic pulse velocity", *Constr. Build. Mater.*, **125**, 1022-1027.

https://doi.org/10.1016/j.conbuildmat.2016.08.158

Sakagami, T. and Kubo, S. (2002), "Development of a new non-destructive testing technique for quantitative evaluations of delamination defects in concrete structures based on phase delay measurement using lock-in thermography", *Infrared Phys. Technol.*, **43**(3), 311-316. https://doi.org/10.1016/S1350-4495(02)00157-3

Samantaray, S.K., Mittal, S.K., Mahapatra, P. and Kumar, S. (2018), "An impedance-based structural health monitoring approach for looseness identification in bolted joint structure", *J. Civil Struct. Health Monitor.*, **8**(5), 809-822. https://doi.org/10.1007/s13349-018-0307-2

Thakur, H.V., Nalawade, S.M., Saxena, Y. and Grattan, K.T.V. (2011), "All-fiber embedded PM-PCF vibration sensor for Structural Health Monitoring of composite", *Sensors Actuators A: Phys.*, **167**(2), 204-212. https://doi.org/10.1016/j.sna.2011.02.008

Trtnik, G., Kavčič, F. and Turk, G. (2009), "Prediction of concrete strength using ultrasonic pulse velocity and artificial neural networks", *Ultrasonics*, **49**(1), 53-60. https://doi.org/10.1016/j.ultras.2008.05.001

Xie, L., Wang, X., Yang, C., Jiang, Y., Liu, Q., Miao, Q. and Chen, X. (2022), "Development and validation of a defect detection and repair method for half grouted sleeve connection", *Case Stud. Constr. Mater.*, **17**, p. e01205. https://doi.org/10.1016/j.cscm.2022.e01205

Xie, X.Y., Cui, Y.G. and Yu, Y. (2024), "Study of nonlinear hysteretic modelling and performance evaluation for piezoelectric actuators based on activation functions", *Smart Struct. Syst., Int. J.*, **33**(2), 133-143. https://doi.org/10.12989/sss.2024.33.2.133

Yue, Z. (2023), "Research on grouting defects of bridge prestress pipe by impact-echo method", *J. Municipal Technol.*, **41**(4), 194-199+205. https://doi.org/10.19922/j.1009-7767.2023.04.194

Zairul, M. (2021), "The recent trends on prefabricated buildings with circular economy (CE) approach", *Cleaner Eng. Technol.*, **4**, p. 100239. https://doi.org/10.1016/j.clet.2021.100239